Titanium alloy corrosion fatigue crack growth rates prediction
Peridynamics based numerical approach

Karpenko, Olena; Oterkus, Selda; Oterkus, Erkan

DOI
10.1016/j.ijfatigue.2022.107023

Publication date
2022

Document Version
Final published version

Published in
International Journal of Fatigue

International Journal of Fatigue 162 (2022) 107023

Contents lists available at ScienceDirect

International Journal of Fatigue

journal homepage: www.elsevier.com/locate/ijfatigue

Titanium alloy corrosion fatigue crack growth rates prediction: Peridynamics based numerical approach

Olena Karpenko [a,b,*], Selda Oterkus [b], Erkan Oterkus [b]

[a] Faculty of Civil Engineering and Geoscience, Delft University of Technology, 2600AA Delft, the Netherlands
[b] Department of Naval Architecture, Ocean and Marine Engineering, University of Strathclyde, 100 Montrose Street, Glasgow G4 0LZ, United Kingdom

ARTICLE INFO

Keywords:
Peridynamics
Corrosion fatigue
Crack growth prediction
Stress corrosion cracking
Hydrogen Embrittlement
Additive Manufacturing

ABSTRACT

This study presents a numerical approach for modelling the Corrosion Fatigue Crack Growth (CFCG) in conventional casting and additively manufactured Ti6Al4V alloys. The proposed numerical model, based on Peridynamics (PD), combines the PD Fatigue Crack Growth (FCG) model and PD diffusion model in order to couple the mechanical and diffusion fields existing in the material due to the impact of environmental fatigue. The mechanical field is responsible for the characterisation of the changes to the structure due to the fatigue loading conditions. The diffusion field is based on the modelling of the adsorbed-hydrogen Stress Corrosion Cracking (SCC), in particular, the Hydrogen Embrittlement (HE) model is considered. The proposed approach has been validated using experimental data available in the literature showing the capability of the tool to predict the CFCG rates.

1. Introduction

The combination of two events of corrosion and fatigue can often be the most dangerous mechanisms of material failure and is known as environmental fatigue or Corrosion Fatigue (CF). Corrosion itself can generate a lot of damage in metals, but the combination of fatigue, can jeopardize the material strength and decrease the structure's life. The effect of environmental fatigue on the failure of metallic structures is summarised in [1].

Corrosion is a complex phenomenon and can be divided into generalized and localized. Generalized corrosion affects uniformly the entire surface of metal exposed to the corrosion environment; instead, the localized corrosion initiates locally. For localized corrosion, initiation can be a very long process, but the growth is rapid once started. The localised corrosion process is often elevated by stresses and is referred to as Stress Corrosion Cracking (SCC). SCC is possible only when the material is under the static or fatigue load and is exposed to an aggressive environment. The combination of material, environment and stress state results in SCC and corrosion crack propagation [1]. Many metals like titanium, stainless steel, high tensile steel, and aluminium alloys are corrosion-resistant but are sensitive to SCC. Primarily it was noticed in the pre-notched metals, where SCC occurs at the notch tip [2]. When the crack is already in the material, it triggers the SCC where the film rupture at the crack tip occurs with the dissolution process taking place. This process commonly occurs due to fatigue when the passivizing oxide film protecting the metal surface ruptures and does not have enough time to re-passivate.

The experimental studies [3–5] on CFCG in conventional casting Ti6Al4V alloys tested in several environments indicated the increase in Fatigue Crack Growth Rates (FCGR) in 3.5 %wt NaCl solution and distilled water, and the frequency-dependent behaviour. A few studies [6,7] were performed on additively manufactured Ti6Al4V alloy, where the corrosion behaviour of Selective Laser Melting (SLM) and wire + arc additive manufacturing (WAAM) Ti6Al4V subjected to 3.5 wt NaCl solution was investigated. The researchers concluded that the effect of microstructure on corrosion resistance where the order of corrosion resistance was identified as SLM < WAAM < rolling < SLM + heat treatment, with pitting corrosion as the main failure mechanism. Regarding the understanding of the contribution of the corrosion on FCG in additively manufactured Ti6Al4V, a very limited number of studies were performed. Jesus et al. [8] performed a study on FCGR in Ti6Al4V specimens produced by SLM under a corrosive environment with the outcome of faster FCG when the tests are performed in 3.5 wt NaCl. Neikter et al. [9] analysed the Ti6Al4V samples produced by Electron Beam Melting (EBM), investigated the Hydrogen Embrittlement (HE) phenomena, and concluded the susceptibility of EBM Ti6Al4V alloys to

* Corresponding author.
E-mail address: o.karpenko@tudelft.nl (O. Karpenko).

https://doi.org/10.1016/j.ijfatigue.2022.107023
Received 6 January 2022; Received in revised form 12 April 2022; Accepted 18 May 2022
Available online 22 May 2022

HE with the increased FCGR.

For the FCG in the corrosive environment, several mechanisms are likely possible. FCG in the air has a characteristic sigmoidal shape of relation between $da/dN - \Delta K$ and occurs above the threshold Stress Intensity Factor (SIF) range ΔK_{th} with further linear dependence of da/dN on ΔK and final rapid growth when SIF is approaching the critical value. Instead, FCG behaviour in a corrosive environment is a more complex process that includes three different categories classified by [10]. All three categories of crack growth depend on the threshold SIF for SCC and can be defined with respect to ΔK_{ISCC}[11]. K_{ISCC} is the threshold phenomenon for SCC, below which the SCC do not occur. K_{ISCC} is the one of the most important parameters of SCC definition and the researches use the threshold SIF for SCC, K_{ISCC}, as a baseline for defining the categories of crack growth. The general block-scheme of CFCG categories, CFCG models and schematics of CFCG curves are presented in Fig. 1, where a_o is the initial crack length and $\Delta\sigma$ is the load amplitude.

Coupling the fatigue with corrosion can be a devastating combination for structural components. CF and CFCG rates are of great interest for the life prediction of engineering structures. McEvily and Wei [10] classified the CFCG with respect to K_{ISCC}, as shown in Fig. 1. In the following classification when $K_{max} < K_{ISCC}$ the fatigue refers as True Corrosion Fatigue (TCF), where the crack growth is increased by environmental effects, for example, filiform, pitting, exfoliation [12] and the CFCG rate is in the form:

$$\left(\frac{da}{dN}\right)_{TCF} = \left(\frac{da}{dN}\right)_{Air} + \left(\frac{da}{dN}\right)_{Pitting} \quad (1)$$

The second category shown in Fig. 1 is SCC, when $K_{max} > K_{ISCC}$, in which the system is more sensitive to stress corrosion and when the ΔK_{ISCC} for corrosion cracking is much lower than the critical SIF, K_C. Generally, the SCC is the result of a combination of 3 factors: exposure to a corrosive environment, susceptible material and tensile stresses above a threshold value [1]. Additionally, the reduction of frequency of the cycles or the increase of the load ratio triggers the SCC mechanism [12,13]. There is no unified mechanism for SCC in the literature. Various models have been proposed, which are based on damage by passive film rupture [14,15], adsorption models [16] when the specific chemicals adsorb on the crack surface and flowerers the fracture stress, and the HE model [5,17–19], where hydrogen atoms diffuse to the crack tip and embrittle the metal. The models in this category are named CF, and two types of models are introduced in the literature: the superposition model [20,21] and the process-competition model [22]. The superposition model was introduced by Wei and Landers [20], where the CFCG rate, $\left(\frac{da}{dN}\right)_{CF}$, is equal to the sum of mechanical FCGR, $\left(\frac{da}{dN}\right)_{Air}$, and the contribution from SCC, $\left(\frac{da}{dN}\right)_{SCC}$:

$$\left(\frac{da}{dN}\right)_{CF} = \left(\frac{da}{dN}\right)_{Air} + \left(\frac{da}{dN}\right)_{SCC} \quad (2)$$

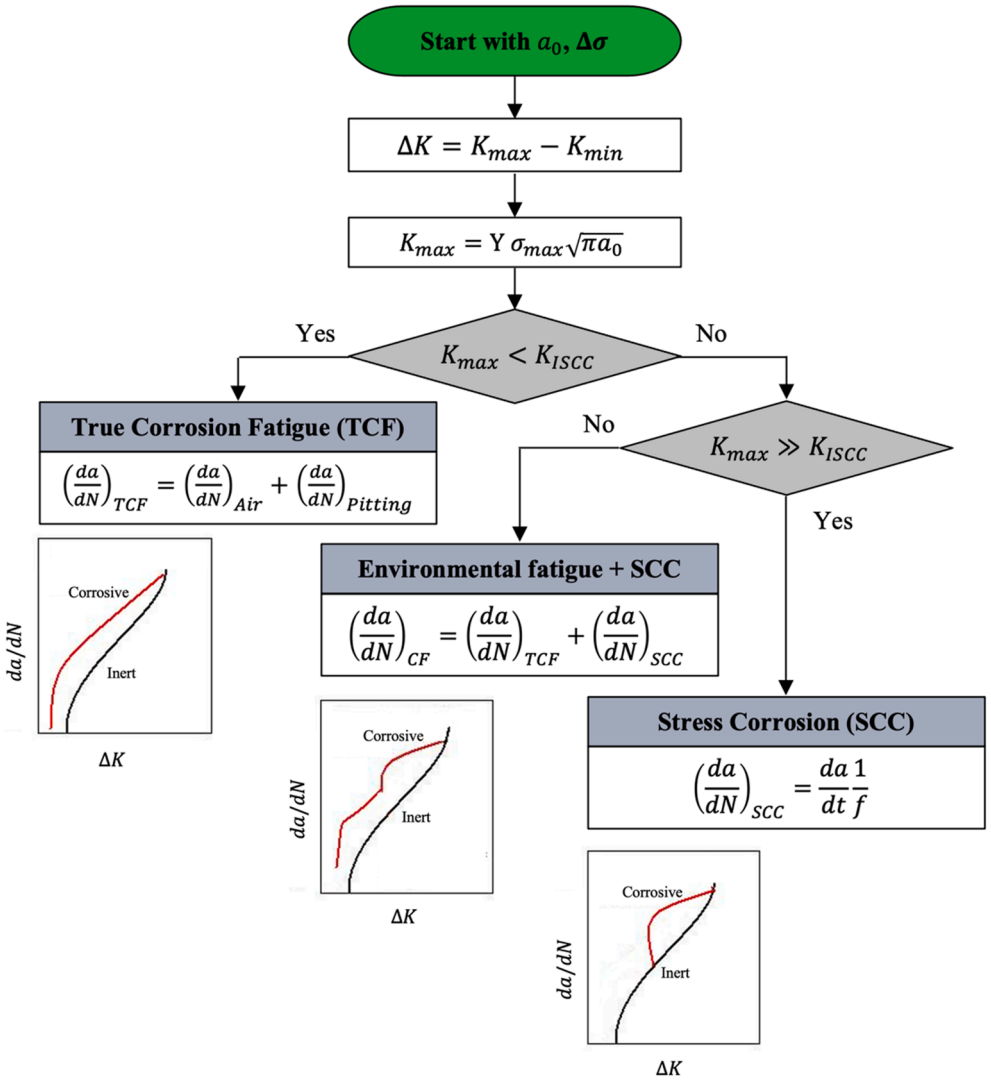

Fig. 1. Block-scheme of CFCG categories.

The SCC is time-dependent, and the shift from da/dN to da/dt can be evaluated in the following form:

$$\left(\frac{da}{dN}\right)_{SCC} = \frac{da}{dt}\frac{1}{f} \tag{3}$$

where f is the frequency of the loading cycle.

Another CF model proposed in [21] is including also the cycle-dependent corrosion term $(da/dN)_{cdc}$:

$$\left(\frac{da}{dN}\right)_{CF} = \left(\frac{da}{dN}\right)_{Air} + \left(\frac{da}{dN}\right)_{cdc} + \left(\frac{da}{dN}\right)_{SCC} \tag{4}$$

The authors in [21] identified several models of $(da/dN)_{cdc}$, but concluded that the process of finding the correct parameters for $(da/dN)_{cdc}$ definition is quite a complicated process.

The competition model proposed in [22] assumes that the CF is equal to the larger of two possible effects:

$$\left(\frac{da}{dN}\right)_{CF} = max\begin{cases}\left(\frac{da}{dN}\right)_{TCF}\\ \left(\frac{da}{dN}\right)_{SCC}\end{cases} \tag{5}$$

Some empirical engineering models [23–26] for CFCG are developed where the researchers take into account the effect of the environment on the FCG and express the CFCG rate as a function of the SIF range. However, most models follow the Paris law type equation by fitting the curves to the experimental data and obtaining the model constants based on a given environment's test data. Instead, a new numerical approach, based on PD, is proposed and discussed in this paper, where the PD FCG model is combined with the PD diffusion model for CFCG rates predictions. The PD diffusion model for a specific SCC HE mechanism is presented in detail. The numerically predicted FCGR are analysed and compared to the test data available in the literature.

2. Method

The failure of the structures can be unpredictable and it is difficult to detect phenomena, especially under the combination of mechanical loads and environmental conditions. The numerical methods commonly used by engineers are mainly based on classical continuum mechanics with the governing equations in the form of partial differential equations. However, such methods become invalid in the presence of field's discontinuities such as cracks, and a new continuum mechanics theory, named Peridynamics [27], was introduced to overcome this limitation. PD is based on integro-differential equations and proved its applicability on fatigue crack nucleation [28], propagation problems in metals [29,30] and composites [31] and on corrosion problems [32,33]. The current research will also show the applicability of the PD tool on the CF problems. The combined PD model is used for CF modelling and CFCG predictions. Section 2.1. provides an overview of the PD fatigue model, Section 2.2 introduces the PD HE model, and Section 2.3 proposes a new approach of combining both models in the PD CF model.

2.1. PD fatigue model

Bond-based PD [27] can be used for the evaluation of the structures' response simulations subjected to fatigue loading. According to the PD formulation, the material point $\boldsymbol{x}$ interacts with the other material points $\boldsymbol{x}'$ within the specified domain, named horizon H_x. H_x is defined for each material point by the radius of the horizon δ, shown in Fig. 2. The PD governing equation can be written as [34]:

$$\rho(\boldsymbol{x})\ddot{\boldsymbol{u}}(\boldsymbol{x},t) = \int_{H_x} \boldsymbol{f}(\boldsymbol{u}(\boldsymbol{x}',t)-\boldsymbol{u}(\boldsymbol{x},t),\boldsymbol{x}'-\boldsymbol{x})dV_{x'} + \boldsymbol{b}(\boldsymbol{x},t) \tag{6}$$

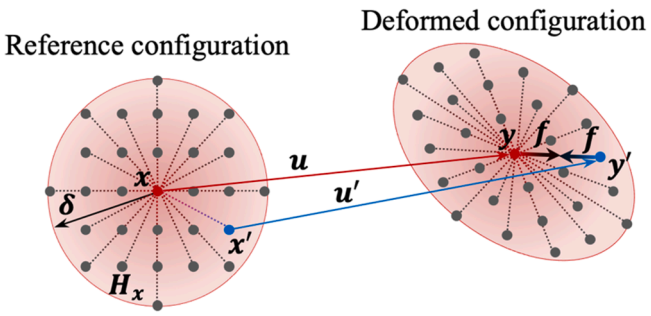

Fig. 2. Bond-based PD forces between two material points.

where $\rho(\boldsymbol{x})$, $\ddot{\boldsymbol{u}}(\boldsymbol{x},t)$ and $\boldsymbol{b}(\boldsymbol{x},t)$ are the mass density, acceleration and body load of the material point $\boldsymbol{x}$ at time t. $dV_{x'}$ is the volume of the material point $\boldsymbol{x}'$. $\boldsymbol{f}(\boldsymbol{u}(\boldsymbol{x}',t)-\boldsymbol{u}(\boldsymbol{x},t),\boldsymbol{x}'-\boldsymbol{x})$ is the pairwise force density, and in case of an elastic material, it is a result of the interactions between material points $\boldsymbol{x}$ and $\boldsymbol{x}'$ and defined as [34]:

$$f = cs\frac{\boldsymbol{y}'-\boldsymbol{y}}{|\boldsymbol{y}'-\boldsymbol{y}|} \tag{7}$$

where $\boldsymbol{y}$ is the location of the material point after deformation, as shown in Fig. 2, c is the micromodulus defined in [35] and s is the stretch parameter between material points which can be expressed as:

$$s = \frac{|\boldsymbol{y}'-\boldsymbol{y}|-|\boldsymbol{x}'-\boldsymbol{x}|}{|\boldsymbol{x}'-\boldsymbol{x}|} \tag{8}$$

The parameter of the critical stretch s_c is introduced in the PD model, which predefines the limit of the bond stretch, at which the bonds between material points can be broken. According to [34], the bonds are broken irreversibly once they are stretched beyond the critical limit, and the bond no longer sustains the tensile force.

Taking into account the cycling loading conditions where the specimen is subjected to a sinusoidal load and cycling between two extremes of F_{min} and F_{max} the PD analysis results in two stretches s^{min} and s^{max}, respectively. Consequently, the cyclic bond can be defined as [36]:

$$\varepsilon = \left|s^{max}-s^{min}\right| = |(1-R)s^{max}| \tag{9}$$

where R is the load ratio and $R = s^{min}/s^{max}$.

Silling and Askari [36] introduced the PD model for fatigue cracks, where the proportionality between the cyclic bond strain ε and cyclic SIF ΔK leads to the relationship between the PD FCG parameters and the Paris law in the following form:

$$\frac{d\lambda(N)}{dN} = -A\varepsilon^m \tag{10}$$

where $\lambda(N)$ is the damage variable called the "remaining life". $\lambda(N)$ is degrading over the fatigue cycles N with the initial value of $\lambda(0)=1$. When $\lambda(N)$ between two points reduces to zero $\lambda(N)\le 0$, the bond is breaking, and fatigue cracking occurs in the structure.

A and m are the PD fatigue parameters which are calibrated by matching $\frac{da}{dN}-\Delta K$ curves with experimental data, as described in [36].

To monitor the accumulated damage of the bonds over the loading cycles N, the local damage φ of each material point is evaluated and defined as:

$$\varphi(\boldsymbol{x},N) = 1-\frac{\int_{H_x}\psi(\boldsymbol{x}'-\boldsymbol{x},N)dV_{x'}}{\int_{H_x}dV_{x'}} \tag{11}$$

where ψ is a history-dependent scalar-valued function to represent broken bonds between material points [37] and can be written as:

$$\psi(\boldsymbol{x}^{'}-\boldsymbol{x},N)=\begin{cases}1 & if\lambda(N)\rangle 0 forall 1<N\\ 0 & otherwise\end{cases} \tag{12}$$

Local damage ranges from 0 to 1. When $\varphi = 0$, all interactions associated with the material point are intact and when $\varphi \geq 0.38$, the crack formed and propagated within the sample.

2.2. PD hydrogen diffusion model

Hydrogen enrichment in the Ti6Al4V is leading to HE with the phenomena observed in multiple studies. Similar to the approach adopted in [33] on hydrogen grain boundary diffusion, in this study, the reduced model [38] of Fisher's mechanism [39] of diffusion is used in the following form:

$$\frac{dC_H}{dt}=D_H\nabla^2 C_H \tag{13}$$

where D_H is hydrogen diffusion coefficient or diffusivity, m^2/s and C_H is the hydrogen concentration. Eq. (13) describes the evolution of C_H in time t. Ti6Al4V can contain mixed phases, which can have different hydrogen diffusivities. The hydrogen diffusion coefficient in α-phase is $D_{H_\alpha}=1.45\times10^{-16}m^2/s$ and for the β-phase is $D_{H_\beta}=5.45\times10^{-12}m^2/s$ at room temperature [40]. According to [18], hydrogen diffusion depends on the microstructure of the titanium, where the hydrogen absorption rate is higher in the microstructures with continuous β-phase. Additionally, in $\alpha+\beta$ alloys, hydrogen prefers to diffuse in β-phase and with an α-phase in the structure hydrogen diffuses along the β/α grain boundaries. For this study, the simulated Ti6Al4V alloys are assumed homogenous and D_{H_β} for β-phase is considered. Please note that the effect of α-phase is neglected together with the microstructural effect on the hydrogen diffusion in this study which may have an effect on the CFCGR. These effects will be considered in a future study.

PD governing equation for hydrogen diffusion mechanism is based on Fisher's model in Eq. (13) and is given in the following form [33]:

$$\dot{C_H}(\boldsymbol{x},t)=\int_{H_x}\boldsymbol{f_H}(C_H(\boldsymbol{x}^{'},t)-C_H(\boldsymbol{x},t),\boldsymbol{x}^{'}-\boldsymbol{x})dV_{x^{'}} \tag{14}$$

where $\dot{C_H}(\boldsymbol{x},t)$ is the time derivative of hydrogen concentration for a material point $\boldsymbol{x}$ and V is the incremental volume of material point $\boldsymbol{x}^{'}$. $\boldsymbol{f_H}$ is the hydrogen diffusion response function and defined as:

$$f_H=d_{bc}\frac{C_H(\boldsymbol{x}^{'},t)-C_H(\boldsymbol{x},t)}{|\boldsymbol{x}^{'}-\boldsymbol{x}|} \tag{15}$$

In Eq. (15), d_{bc} is the diffusion bond constant, which can be expressed as [33]:

$$d_{bc}=\frac{6D_H}{\pi h\delta^3} \tag{16}$$

where δ is the horizon size.

The hydrogen diffusion model is simulated in the time domain where the backward difference method is used to obtain hydrogen concentration for the next time step n_{t+1}:

$$C_{H(i)}^{n_t+1}=C_{H(i)}^{n_t}+\dot{C}_{H(i)}^{n_t+1}\Delta t \tag{17}$$

where Δt is the time step size which can be expressed in terms of cyclic period $T=1/f$ (f is the frequency, Hz) and the total number of time steps n_F within one period:

$$\Delta t=\frac{T}{n_F} \tag{18}$$

To represent the hydrogen adsorption in the sample, the concept of hydrogen coverage θ_H is introduced in the PD diffusion model [33]:

$$\theta_H=\frac{C_{Htip}}{C_{Hsat}} \tag{19}$$

where C_{Htip} is the surface hydrogen concentration at the crack tip and C_{Hsat} is the surface hydrogen concentration saturation value.

2.3. Coupling of mechanical and diffusion fields

The coupling of mechanical and diffusion fields is necessary to identify the effect of hydrogen on material strength and susceptibility of Ti6Al4V to hydrogen-induced cracking. With this respect, the test data [41] was considered, where the decrease of critical SIF was noticed with the increased hydrogen level in the material. The test data is adapted and presented in Fig. 3a, indicating the sample embrittlement. For the purpose of integrating the phenomena of local embrittlement in the material as hydrogen is adsorbed and diffused within the sample, the hydrogen-embrittlement model is adopted.

In the PD model, the influence of hydrogen is accounted by a decrease of a critical stretch s_c with increasing hydrogen coverage θ_H. To find the coupling between θ_H and dependent s_c, Langmuir-McLean isotherm [42] is utilised, which relates hydrogen coverage to the bulk hydrogen concentration C_H (unit mol H/mol Ti) in the following form:

$$\theta_H=\frac{C_H}{C_H+\exp\left(-\Delta G_b^0/RT\right)} \tag{20}$$

where ΔG_b^0 is the Gibbs energy difference between surface and bulk material, and in the current model is the trapping energy of hydrogen at a Ti grain boundary, $\Delta G_b^0 = 40kJ/mol$, R and T are gas constant and absolute temperature, respectively.

As shown in Fig. 3b, utilising Eq. (20) to convert test data to the relation between the θ_H and s_c, resulted in the following equation:

$$K_c(\theta_H)=5.4\theta_H^{-0.409} \tag{21}$$

And for a 2-Dimensional problem, $s_c(\theta_H)$ in connection with the material fracture energy G_c is evaluated by [43]:

$$s_c(\theta_H)=\sqrt{\frac{5\pi G_c(\theta_H)}{12E\delta}} \tag{22}$$

where E is Young's modulus, G_c can be calculated for a plane strain configuration according to the critical SIF:

$$G_c(\theta_H)=\frac{K_c(\theta_H)^2}{E/(1-\upsilon^2)} \tag{23}$$

The study [41] indicates the effect of the strain rates on the hydrogen embrittlement process. It is suggested that during slower rates with a longer time, creep deformation occurs. With added hydrogen to the samples, the embrittlement occurred at the lower hydrogen content, compared to the samples strained at faster rates. This means that slower rates of the applied loads resulted in the loss of the overall ductility and increased embrittlement process due to hydrogen.

The important effect of the load frequency is noticed during FCGR tests on Ti6Al4V alloys, where low-frequency fatigue is more sensitive to the environment. To consider the effect of the load frequency on the hydrogen embrittlement process, the following relationship is introduced in the PD model:

$$K_c(\theta_H)=\frac{K_{Ic}(1-R)}{\Delta K_{scc}}\theta_H^{-0.409} \tag{24}$$

where K_{Ic} is the critical SIF, which is selected for Ti6Al4V as $K_{Ic}=105MPa\sqrt{m}$, and ΔK_{scc} is selected from the available test data [44]: $\Delta K_{Iscc}=17.6MPa\sqrt{m}(f=1Hz)$, $\Delta K_{Iscc}=13.2MPa\sqrt{m}(f=5Hz)$ and $\Delta K_{Iscc}=11.0MPa\sqrt{m}(f=10Hz)$. Fig. 4 shows the critical stretch values as a function of θ_H for different load frequencies. The relation in Eq. (24)

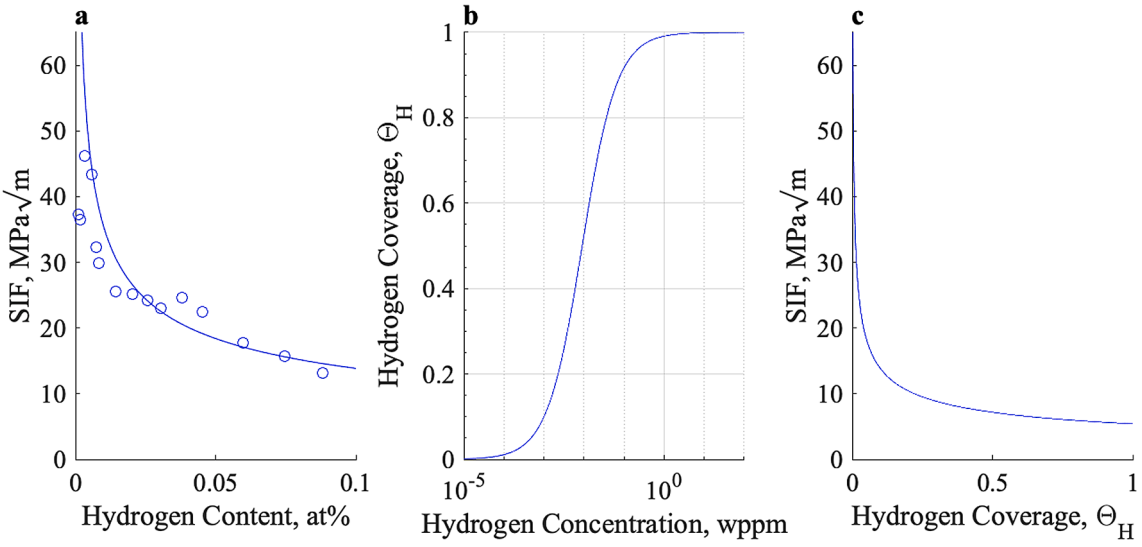

Fig. 3. a. Effect of Hydrogen content on the critical SIF, adapted from [41], b. Hydrogen Coverage, θ_H as a function of Hydrogen Concentration [42] for $\Delta G_b^0 = 40kJ/mol$, c. SIF as a function of θ_H.

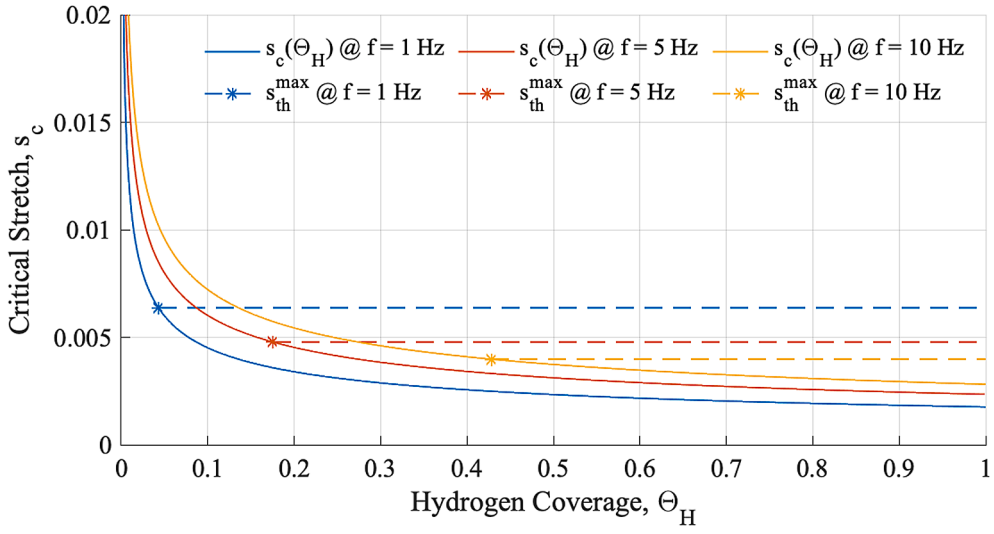

Fig. 4. Variation of critical stretch with hydrogen coverage.

effects on crack propagation, where at the same amount of hydrogen coverage in the metal, the fatigue progression of the crack is faster at low-frequencies, as shown in Fig. 4. With the following assumption, the study in Section 5 shows the effect of the frequencies in CFCGR, where after the $K_c(\theta_H)$ reaches the ΔK_{Iscc}, the differences of FCGR for different frequencies are noticeable. If the relationship in Eq. (24) is not introduced, then the frequency effect is not visible, and CFCGR will be the same for all frequencies.

Moreover, to take into account that the SCC occurs when $\Delta K > \Delta K_{ISCC}$ with abrupt changes in the behaviour of $log(\frac{da}{dN}) - \log(\Delta K)$, the K_{th}^{max} value is introduced in the model, below which the crack growth is not occurring due to SCC. For the given load frequency, the K_{th}^{max} is determined from the test data, where:

$$K_{th}^{max} = \frac{\Delta K_{Iscc}}{(1-R)} \tag{25}$$

The resulting plots can be seen in Fig. 4, where the critical stretch decreases with the increase in hydrogen concentration, evaluated by Eq. (24). And when the stretch of the bond is $s < s_{th}^{max}$ (s_{th}^{max} evaluated from K_{th}^{max} by Eq. (22)), then there is no effect of HE process, and the bonds are breaking only by the decreasing life over the fatigue cycles, as explained in Section 2.1.

3. PD CFCG model procedure

In the current studies for CFCG prediction in C(T) titanium alloy samples, PD is utilised as the main numerical tool. According to the corrosion fatigue model proposed by Wei and Landers [20] for the CFCG, $(\frac{da}{dN})_{CF}$, CFCG is the sum of the mechanical FCGR, $(\frac{da}{dN})_{Air}$, and the contribution from the SCC, $(\frac{da}{dN})_{SCC}$. The following CFCG model is developed utilising the PD numerical model, where Fig. 5 shows the general scheme of the model when Compact Tension C(T) sample is with the crack length of a_0 and the load of ΔF is applied. The model is classified relative to the $K_c(\theta_H)$. When $K_{max} < K_c(\theta_H)$, then $(\frac{da}{dN})_{CF} = (\frac{da}{dN})_{Air}$. When $K_{max} > K_c(\theta_H)$, then $(\frac{da}{dN})_{CF}$ is a result of interaction between the mechanical fatigue and time-dependent corrosion contribution, $(\frac{da}{dN})_{CF} = (\frac{da}{dN})_{Air} + (\frac{da}{dN})_{SCC}$. The environmental contribution is set up as a HE model, and FCG is in the air considering the effect of the environmental-assisted crack growth. And when $K_{max} \gg K_c(\theta_H)$, the crack growth is

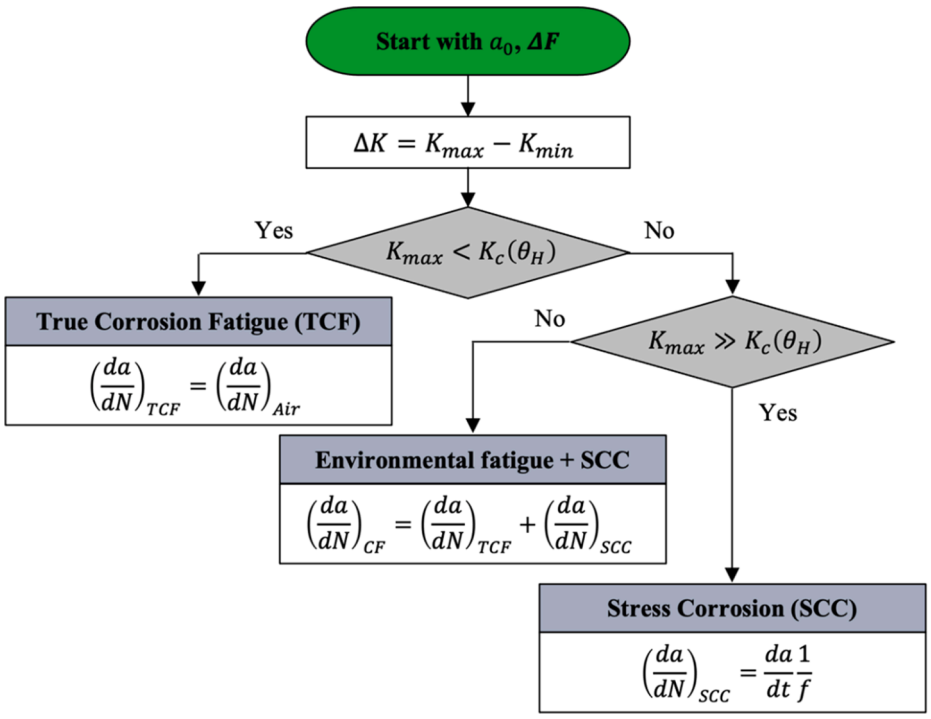

Fig. 5. Block-scheme of CFCG categories in PD model.

occurring due to the HE and SCC is the main contributor to the failure.

In this respect, the PD model is set up for fatigue damage predictions, which is $(da/dN)_{Air}$ and numerical diffusion model, which is the HE model, $(da/dN)_{SCC}$. Both models have to be integrated to predict the CFCG and Fig. 6 shows the three stages of the PD model:

1. PD model initiation and parameters identification: model preparation, discretisation, assignment of the material properties, identification of the fatigue and diffusion model parameters, identification and assignment of the fatigue loads.

2. PD hydrogen embrittlement model.

2.1 Hydrogen coverage step: assignment of the unit value of the hydrogen coverage, $\Theta_H = 1$, at the crack tip and zero value $\Theta_H = 0$ is assigned for all remaining surfaces of the specimen. The unit value of hydrogen coverage corresponds to saturated hydrogen surface concentration of $6549 mol/m^3$.

2.2 Diffusion step: PD hydrogen diffusion model described in Section 2.2. is used to predict the hydrogen diffusion in the material at each time step.

2.3 Embrittlement step: relation in Fig. 3 is used to quantify the local hydrogen concentration on the material strength. The relation between the hydrogen concentration and hydrogen coverage is used to evaluate the critical stretch of the bond, $s_c(\Theta_H)$, as shown in Fig. 4. The bond is broken if the stretch of the bond is greater than the current critical stretch, $s_c > s_c(\Theta_H)$.

3. PD fatigue model: static solutions for the extreme loads and the degrading life of the bonds over the cycles. The bond is broken when its remaining life is $\lambda^N \leq 0$.

During Stage 2 and Stage 3, the accumulated damage of the bonds is monitored, and if the local damage occurs at any of the two stages, then the algorithm moves to the beginning of Stage 2 with the location of the new position of the crack tip and the processes of Stages 2 and Stage 3 repeat until the full damage of the sample. As the crack propagates, the constant unit value of hydrogen coverage is applied at the new crack tip and the hydrogen concentrations at the crack surfaces.

4. PD CFCG model set up

4.1. Problem set up

Similar to the experimental study [45], the Ti6Al4V samples are subjected to cyclic loading in NaCl solution, the PD model is set up for a C(T) sample, as shown in Fig. 7, subjected to a cyclic load amplitude of $F_a = 2.25 kN$ with a load ratio of $R = 0.1$. The material properties of Ti6Al4V are homogeneous and specified as: Young's modulus $E = 110 GPa$ and Poisson's ratio $\nu = 1/4$.

The following dimensions of the C(T) specimen are considered: width of $W_n = 30 \times 10^{-3} m$, length of $L = 31.25 \times 10^{-3} m$, the thickness of $h = 5 \times 10^{-3} m$ and the length of pre-notch is $a_n = 12.4 \times 10^{-3} m$. The load is applied on the pins with the diameter of $d = 6.25 \times 10^{-3} m$ as a body force density [35] in the following form:

$$b_y = \frac{F_y}{\Delta V_\Delta} \tag{26}$$

where ΔV_Δ is the volume of the pin area, and F_y is the applied tension/compression load, which is defined as:

$$F_y = \begin{cases} F_y^{max} = \dfrac{2F_a}{1-R} \\ F_y^{min} = F_y^{max} R \end{cases} \tag{27}$$

where F_y^{max} and F_y^{min} are the cyclic load extremes.

PD model of C(T) sample is discretised with 10,400 material points with uniform spacing between them $\Delta x = 0.3 \times 10^{-3}$ m and horizon size of $\delta = 3.015 \Delta x$.

The results of FCGR in NaCl solution are compared to the FCGR in the air, where the authors [45] showcased that the fatigue behaviour in the air is frequency independent. Instead, the samples tested in NaCl solution showed frequency dependence with the abrupt increase of FCGR. For this reason, numerically, it is beneficial to look at the complex corrosion-fatigue phenomenon. Firstly, the numerical model set-up is performed for Ti6Al4V in the air, which is described in Section 4.2. Secondly, the fatigue load determination for SCC is described in Section

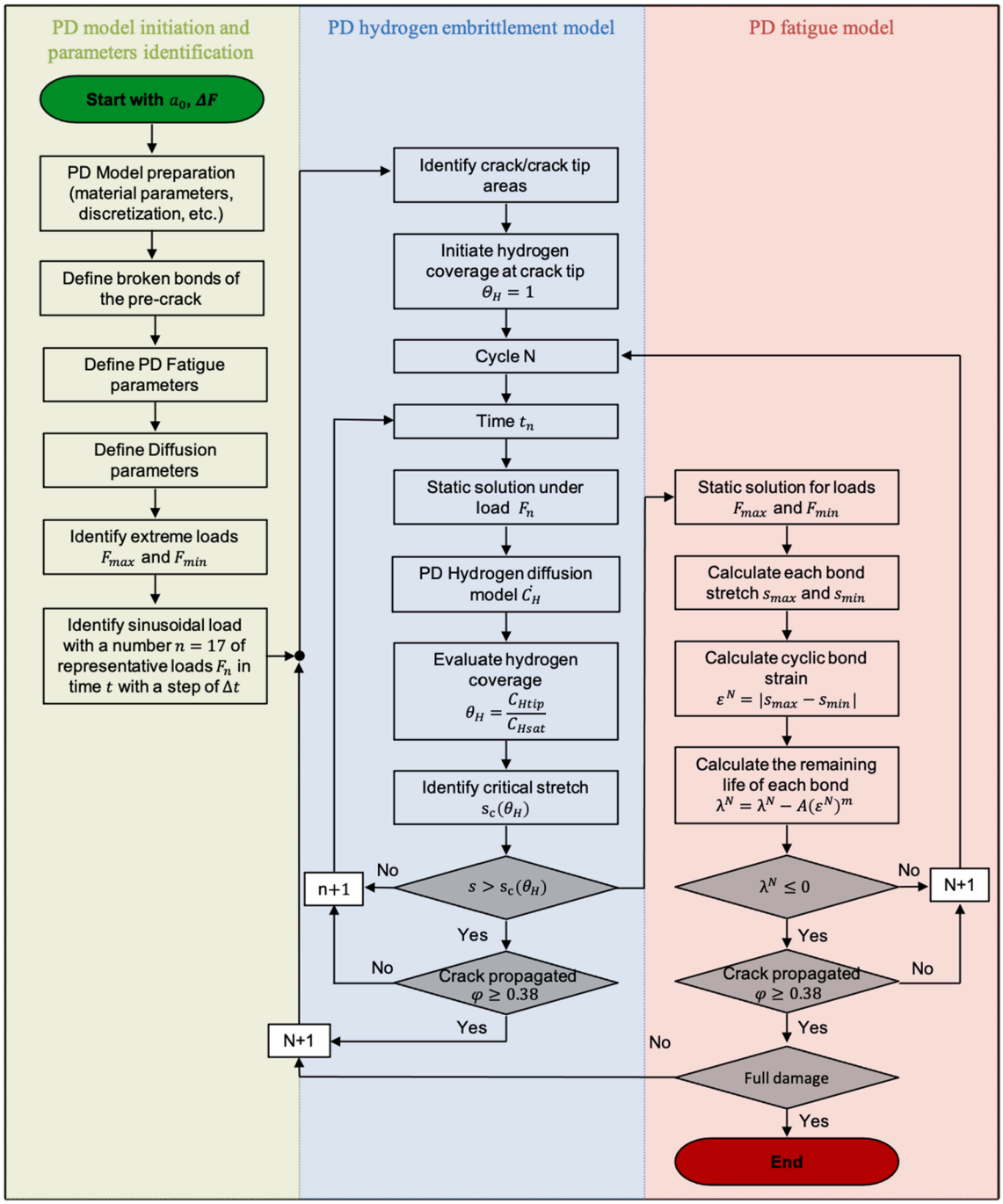

Fig. 6. Solution procedure.

4.3. And lastly, hydrogen diffusion plots are presented in Section 4.4.

4.2. PD FCG model in the air

As discussed in Section 2.1, in the PD fatigue model, the parameters A and m have to be calibrated using the Paris' law data [46]. For this purpose, the data in [45] for the sample tested in the air is selected, where the constant m is obtained directly from the $log\left(\frac{da}{dN}\right) - \log(\Delta K)$ curve, and A is identified by running first model with random parameter A' and then calibrated following the procedure discussed in [36].

After the calibration procedure, the PD FCG model parameters are $A = 22 \times 10^3$ and $m = 3.87$ and the computed results of $log\left(\frac{da}{dN}\right) - \log(\Delta K)$ are in line with the experimental data, shown in Fig. 8. It means that the parameters for the PD FCGR model are set up correctly, and the model tested in the air can be used as a reference one for the next studies.

4.3. Fatigue load determination for PD SCC model

For the sinusoidal waveform employed in the current study, it is assumed that the loading cycle starts from the minimum load of F_{min}:

$$F = \frac{F_{max} - F_{min}}{2} + \frac{\Delta F}{2}\sin\left(2\pi\omega t - \frac{\pi}{2}\right) = \frac{\Delta F}{2}\left[\frac{1+R}{1-R} + \sin\left(2\pi\omega t - \frac{\pi}{2}\right)\right] \tag{28}$$

where ω is the loading frequency, t is the time, R is a load ratio, and ΔF is

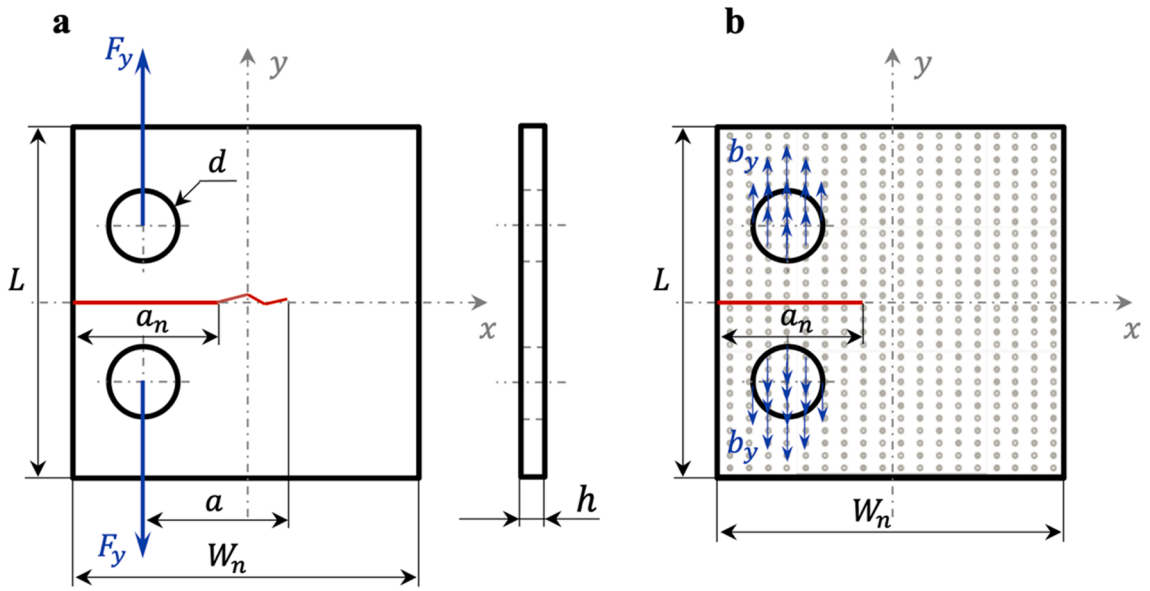

Fig. 7. **a** Square titanium alloy C(T) plate under uniaxial tensile loading and **b** its PD model discretisation.

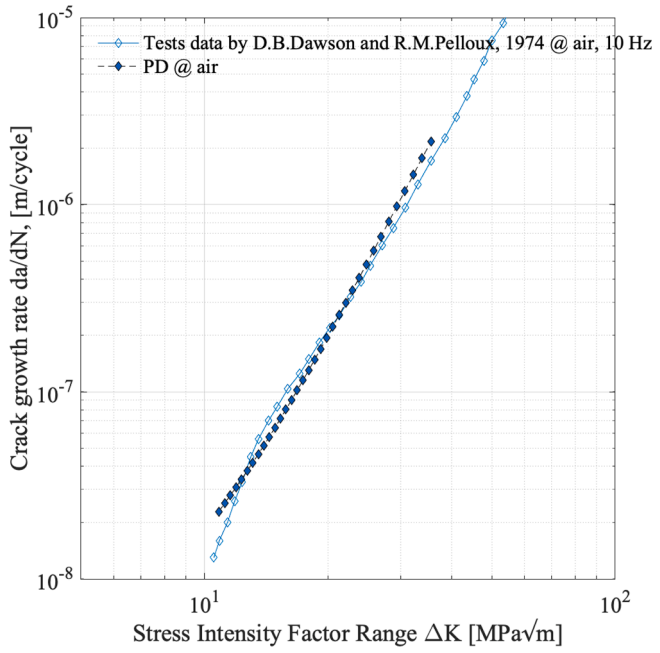

Fig. 8. FCGR versus SIF range for a sample tested in the air.

force range, $\Delta F = F_{max} - F_{min}$.

For metals, such as high strength steels, titanium alloys, mostly attributed to hydrogen embrittlement ahead of the crack tip, the diffusion of hydrogen into the material is produced by an anodic reaction at the crack tip [40]. The process is time-dependent, and the frequency of the cyclic loading affects the FCG. Due to this, the analysis for SCC is performed in the time domain, as shown in Fig. 6, and the plate is subjected to the sinusoidal load. As it is time-consuming to solve the PD under a very small load time-step, the effect of the time-step size, dt on FCGR is analysed. Four time-step sizes are selected: $dt = 0.5, 0.25, 0.125 \text{and} 0.0625 sec$, as shown in Fig. 9. The smaller the time-step size is, the better representation of the sinusoidal load, but the longer the simulations are.

Additionally, to optimise the simulation time, the displacements u (in x-direction) and v (in y-direction) are solved only for half of the period $T/2$ and the resultant displacements are mirrored for the other half of the period. This means that for a period of T, for example, with $dt = 0.0625 sec$ shown in Fig. 10b, forces $F_6 = F_{12}$ and displacements $u(F_6) = u(F_{12})$, $v(F_6) = v(F_{12})$. The resultant displacements are stored for each force within a period and called at each cycle. If damage occurs at any of the forces F_t at step dt within the period T, then the displacements are recalculated.

The simulations for evaluation of the influence of the time-step size on CFCG rates are performed for a cyclic load amplitude of $F_a = 3.15 kN$ with a load ratio of $R = 0.1$ and loading frequency of 1 Hz. Fig. 11 shows the results of the simulations where the model with the smallest time-step size of $dt = 0.0625 sec$ is selected as a reference one (black line at the plot) and the other models with $dt = 0.5, 0.25 \text{and} 0.125 sec$ are compared with it. It can be noted that the differences in FCGR are almost unnoticeable, even for the $dt = 0.05 sec$ when the simulations are performed under the load extremes of F_{max} and F_{min}. Due to this, $dt = 0.05 sec$ is selected for further simulations in order to optimize the computational time, and the simulations for the HE step are simulated in time domain under the loads of F_{max} and F_{min}.

4.4. PD hydrogen diffusion model

Fig. 12 shows hydrogen coverage plots for loading of $F_a = 2.25 kN$ and three frequencies of $f = 1, 5 and 10 Hz$ when fracture initiation occurs in the pre-cracked C(T) sample. The highest level of hydrogen concentration is at the crack tip, where the unit value of hydrogen coverage was initiated.

With the damage model introduced in Section 2.3, where the critical stretch of the bonds is degrading with the increased hydrogen concentration and also affected by the loading frequency, lower hydrogen diffusion time to initiate the fracture is necessary for a higher frequency of $f = 10 Hz$.

5. PD CFCG predictions

5.1. Cast Ti6Al4V alloy

As discussed in Section 2.3, when $\Delta K > \Delta K_{ISCC}$ an abrupt change in behaviour of $log(da/dN) - \log(\Delta K)$ curve takes place with higher FCGR at lower frequencies. Such behaviour was noticed during the experiments performed on cast Ti6Al4V [47] in 3.5 wt% NaCl solution where the results of FCGR showed frequency dependency. The experimental

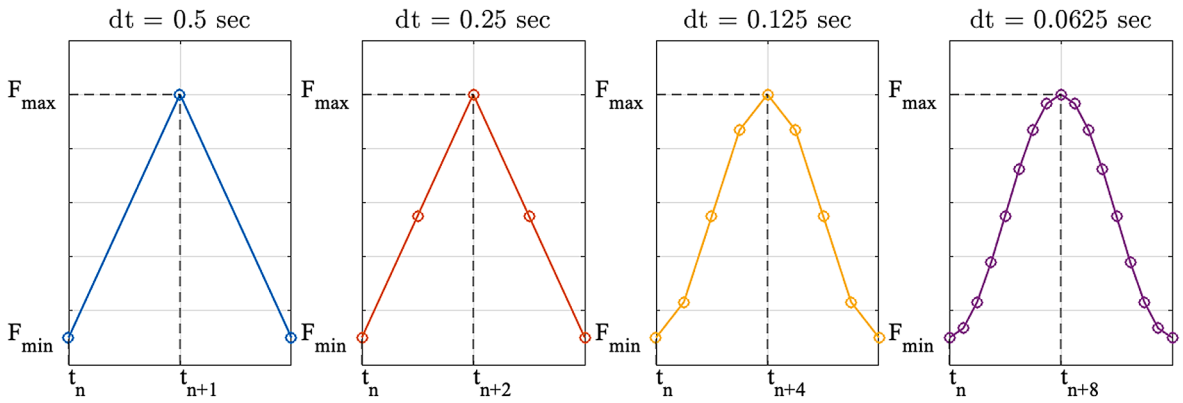

Fig. 9. Load initiation according to a time-step size.

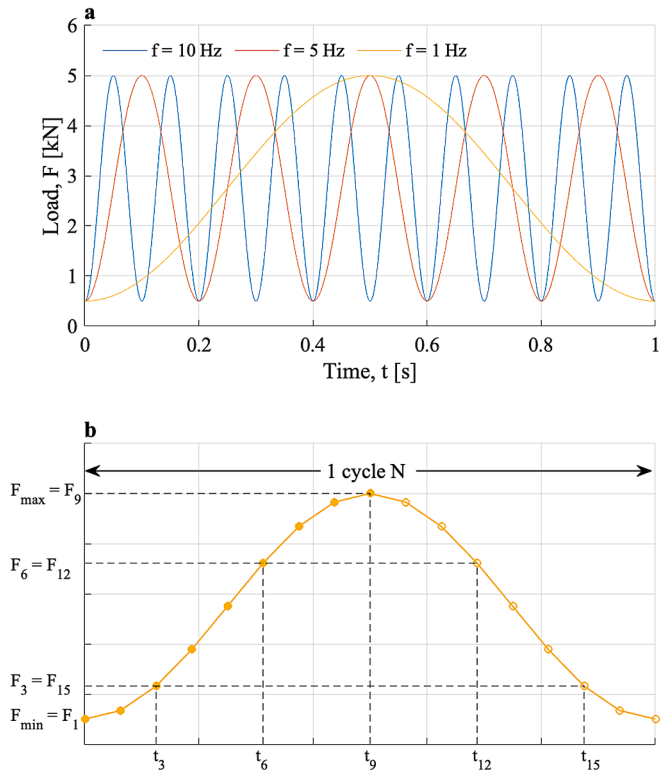

Fig. 10. (a) Load vs time for different loading frequencies; (b) Discretisation of the sinusoidal load F under frequency of $f = 1Hz$ by a time-step of $dt = 0.0625sec$.

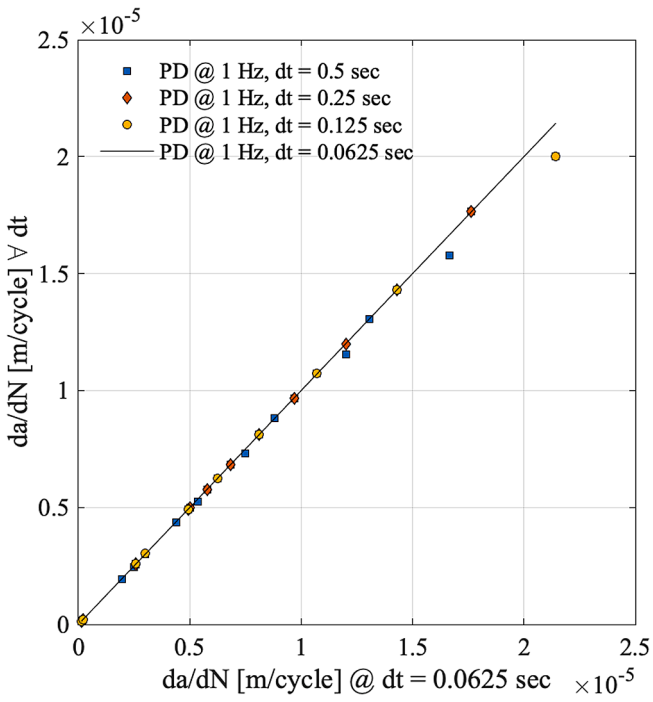

Fig. 11. Comparison between four different time-step sizes.

results indicated that the cyclic SCC occurred when $\Delta K > \Delta K_{ISCC}$. The studies showed that at higher ΔK FCGR accelerate rapidly as ΔK_{ISCC} is approached.

The current study predicts the CFCG rates under different frequencies by the developed numerical PD CFCG model as shown in Fig. 6. The PD model set-up is described in Section 4.1 with a reference model (cast Ti6Al4V in the air) from Section 4.2.

Fig. 13 shows the comparison between the PD CFCG rates and test results by [47] concerning the effect of the loading frequency on CFCG rates. The results of the PD model showed good predictability of the effect of the frequency on corrosion fatigue behaviour of Ti6Al4V alloy. The application of three different frequencies showed three trends of corrosion-fatigue behaviour described in Fig. 5, and that CFCG rates of Ti6Al4V alloy are frequency-dependent. It can be noticed from Fig. 13 that low-frequency fatigue is more sensitive to the corrosive environment, showing the abrupt changes to FCGR with a higher FCGR when $\Delta K > \Delta K_{SCC}$.

The introduced HE model and integration of the HE model in the PD fatigue model showed the capability of the presented PD CFRG model to capture the main features of the complex interaction between the cycling loading, loading frequency and environment.

5.2. Additively manufactured Ti6Al4V alloy

As discussed in [48], the difference between the cast/wrought and additively manufactured Ti6Al4V alloys is the anisotropy of additively manufactured alloys, for example, when the load is applied parallel or perpendicular to the built direction. The anisotropy can be a consequence of residual stresses [30], defects and columnar grains in the additively manufactured materials. Each factor in the structure contributes to reduced fatigue properties and decreases the fatigue life. The limited number of studies [9,49] performed on additively manufactured Ti6Al4V alloy in the corrosive environment showed that hydrogen absorbs and diffuses in the structure and HE mechanism takes place. It is also concluded that the microstructure, like grain size and phase distribution, affects ΔK_{ISCC} and the EBM built Ti6Al4V [9] has $\Delta K_{ISCC} =$

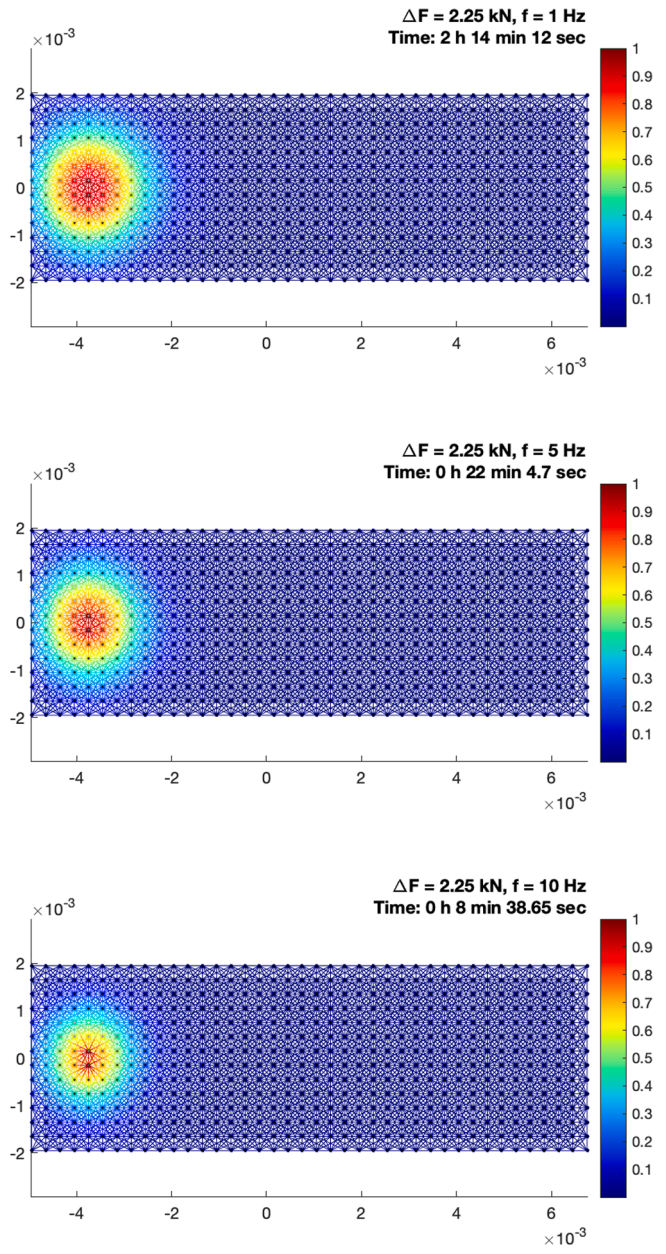

Fig. 12. Hydrogen coverage field at the crack propagation initiation for loading frequencies of $f = 1, 5 \text{and} 10 Hz$.

$23 MPa\sqrt{m}$ tested under the load frequency of $f = 0.5 Hz$ and load rate of $R = 0$. Additionally, other studies concluded that the presence of stresses and temperature also determines the diffusion of hydrogen in the material. But, due to the lack of studies on CFCG of additively manufactured Ti6Al4V alloys and data related to the tested samples anisotropy, it is not possible to validate the developed numerical model. Therefore, some simplifications are considered.

As for the cast Ti6Al4V, it is assumed that the additively manufactured Ti6Al4V alloy is homogenous with the diffusion properties described in Section 2.2. The tests performed in the air on SLM [49] and EBM [9] Ti6Al4V alloys are considered as reference models in order to calibrate the PD FCG model parameters A and m. After the performed calibration process, $A = 550$, $m = 3.0$ for SLM Ti6Al4V tested in the air, and $A = 350$, $m = 3.0$ for EBM Ti6Al4V tested in the air. The PD FCGR with the calibrated parameters are plotted against the test data in Fig. 14, where a good match can be noticed.

Utilising the proposed numerical model with the combined fatigue

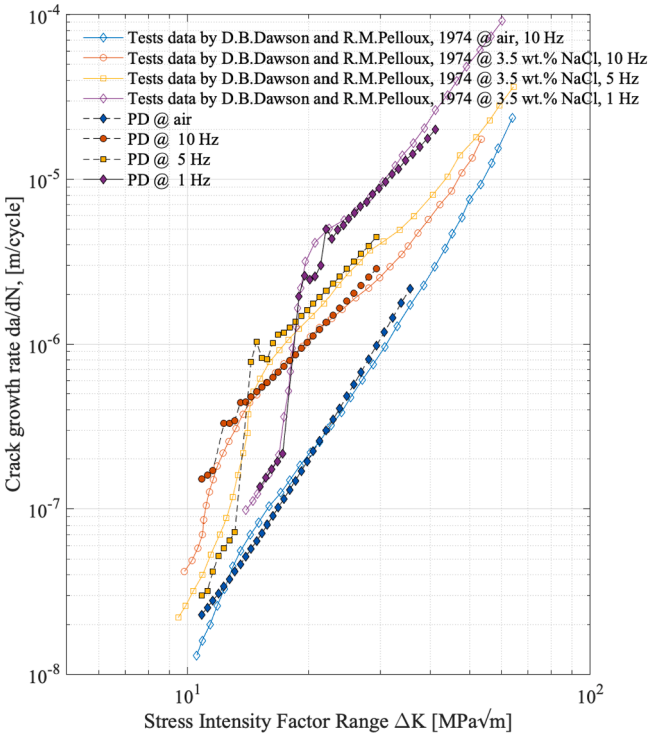

Fig. 13. Effect of loading frequency on CFCG and crack growth curves comparison for a cast Ti6Al4V C(T)-samples between tests data [47] and PD CFCG model.

and hydrogen diffusion model, both structures (SLM Ti6Al4V and EBM Ti6Al4V) are solved with the HE mechanism taking place, as discussed in Section 2.3. The SLM Ti6Al4V C(T) samples are analysed under the load amplitude of $F_a = 2.25 kN$, load frequency of $f = 10 Hz$, load rate of $R = 0.05$, and the EBM Ti6Al4V C(T) are subjected to the cyclic load amplitude of $F_a = 3.15 kN$, load frequency of $f = 0.5 Hz$, load rate of $R = 0$.

Fig. 14 shows the comparison between the CFCG rates of numerical model and experiments [9,49] concerning the relationship between the crack growth rate da/dN and SIF range ΔK. The numerical results are in a good agreement with the expected CFCG in the structure reported by experimental results.

For SLM and EBM Ti6Al4V alloys, tested in the air, the FCG rates followed the Paris law. Instead, the samples exposed to the environmental effects with the hydrogen diffusion ahead of the crack tip, the material experience HE mechanism and has faster crack propagation in the structure. The FCGR of EBM Ti6Al4V alloy rapidly increased at $\Delta K_{ISCC} = 23 MPa\sqrt{m}$ and the FCGR are higher compared to the sample tested in the air.

The proposed PD CFCG model is capable of capturing the fatigue response of the additively manufactured Ti6Al4V alloys affected by a corrosive environment.

6. Conclusion

In this study, the authors present the numerical approach of modelling the fatigue response of metals affected by a corrosive environment. A numerical model combines mechanical and diffusion fields in order to capture the behaviour of the structure due to the applied cyclic loading and SCC phenomena. Considering the Ti6Al4V alloy for the study, a very common phenomenon in the titanium alloys subjected to SCC is HE, and numerical modelling is performed for adsorbed-hydrogen SCC.

Firstly, the proposed CFCG PD model is applied for the cast/wrought

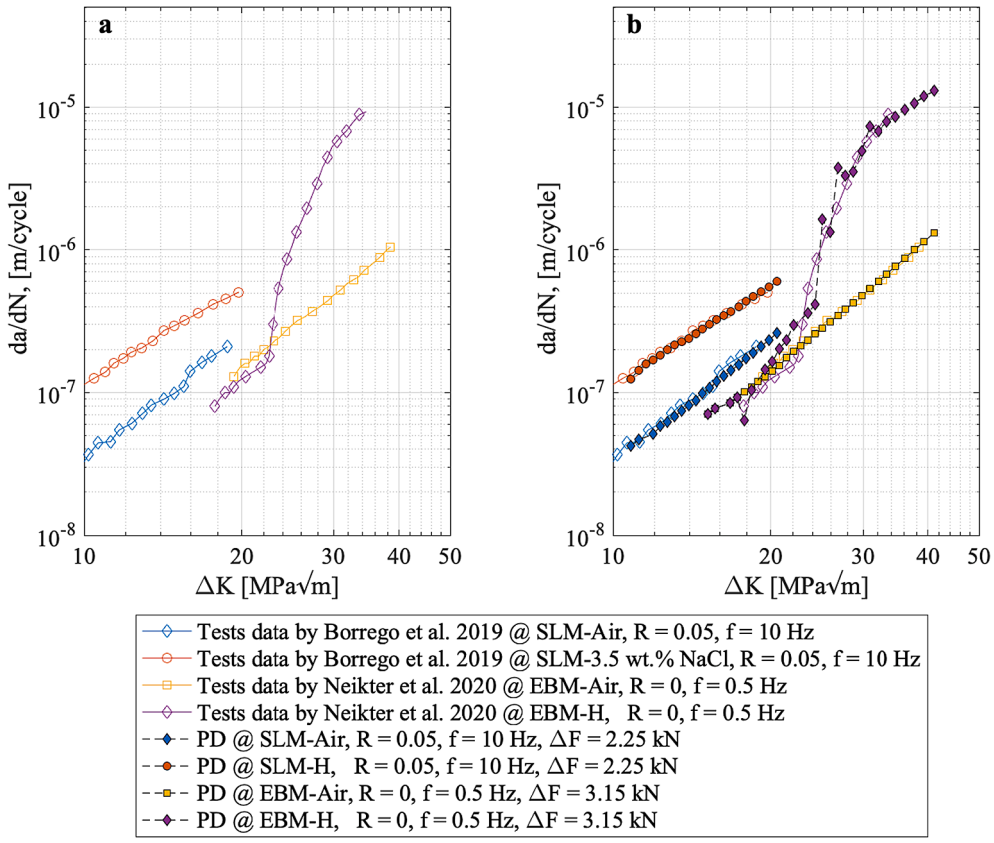

Fig. 14. Crack growth curves comparison for a cast Ti6Al4V C(T)-samples between tests data [47] and PD CFCG model.

Ti6Al4V and validated with the experimental data available in the literature. As multiple studies indicated the effect of the loading frequency on the fatigue performance of the Ti6Al4V, the CFCG rates are analysed for three frequencies. The CFCG rates calculated by PD are in good agreement with experimental data. The combination of cycling loading and the corrosive environment in PD model is capable of capturing the complex fracture behaviour in Ti6Al4V observed in experiments.

Secondly, the proposed PD CFCG model is applied to additively manufactured Ti6Al4V. Due to the lack of data on material structure and the fatigue tests performed on the alloy subjected to the corrosive environment, the simplifications in the PD model are applied. The material is treated as homogenous, so the effects of the material anisotropy (microstructure and residual stresses), as well as the porosities are neglected. After the calibration of the PD parameters of the fatigue model for SLM and EBM Ti6Al4V alloys tested in the air, the PD CFCG model showed good predictability of the material behaviour in the corrosive environment.

Declaration of Competing Interest

The authors declare that they have no known competing financial interests or personal relationships that could have appeared to influence the work reported in this paper.

References

[1] Milella PP, editor. Fatigue and Corrosion in Metals. Milano: Springer Milan; 2013.
[2] Steigerwald EA. Delayed Failure of High Strength Steel in Liquid Environments. Proc ASTM 1960;60:750.
[3] Christ H-J, Senemmar A, Decker M, Prü\ner K. Effect of hydrogen on mechanical properties of β-titanium alloys 2003;28(3-4):453–65.
[4] Baragetti S. Corrosion fatigue behaviour of Ti-6Al-4V in methanol environment. Surf Interface Anal 2013;45:1654–8. https://doi.org/10.1002/sia.5203.
[5] Beachem CD. A new model for hydrogen-assisted cracking (hydrogen "embrittlement"). Metall Trans 1972;3:441–55. https://doi.org/10.1007/BF02642048.
[6] Dai N, Zhang L-C, Zhang J, Zhang X, Ni Q, Chen Y, et al. Distinction in corrosion resistance of selective laser melted Ti-6Al-4V alloy on different planes. Corros Sci 2016;111:703–10.
[7] Yang J, Yang H, Yu H, Wang Z, Zeng X. Corrosion Behavior of Additive Manufactured Ti-6Al-4V Alloy in NaCl Solution. Metall Mater Trans A Phys Metall Mater Sci 2017;48:3583–93. https://doi.org/10.1007/s11661-017-4087-9.
[8] Jesus JS, Borrego LP, Ferreira JAM, Costa JD, Capela C. Fatigue crack growth under corrosive environments of Ti-6Al-4V specimens produced by SLM. Eng Fail Anal 2020;118:104852. https://doi.org/10.1016/j.engfailanal.2020.104852.
[9] Neikter M, Colliander M, de Andrade Schwerz C, Hansson T, Åkerfeldt P, Pederson R, et al. Fatigue crack growth of electron beam melted TI-6AL-4V in high-pressure hydrogen. Materials (Basel) 2020;13. https://doi.org/10.3390/ma13061287.
[10] McEvily A, Wei R. Fracture mechanics and corrosion fatigue. Corros Fatigue Chem Mech Microstruct NACE-2 1972.
[11] Smith HR, Piper DE, Downey FK. A sudy of stress-corrosion cracking by wedge-force loading. Eng Fract Mech 1967:123–8.
[12] Baboian R, Schully J, Gangloff R. Chapter 26—Environmental Cracking-Corrosion Fatigue. Corros Tests Stand Appl Interpret Ed 2009:302-302–20. 10.1520/mnl11032m.
[13] Donahue JR, Lass AB, Burns JT. The interaction of corrosion fatigue and stress-corrosion cracking in a precipitation-hardened martensitic stainless steel. npj Mater Degrad 2017;1(1).
[14] Nelson HG. A film-rupture model of hydrogen-induced, slow crack growth in acicular alpha-beta titanium. Metall Trans A 1976;7:621–7. https://doi.org/10.1007/BF02646469.
[15] Hull D. Effect of crazes on the propagation of cracks in polystyrene. J Mater Sci 1970;5:357–63. https://doi.org/10.1007/BF02397790.
[16] Largitte L, Pasquier R. A review of the kinetics adsorption models and their application to the adsorption of lead by an activated carbon. Chem Eng Res Des 2016;109:495–504. https://doi.org/10.1016/j.cherd.2016.02.006.
[17] Alvarez AM, Robertson IM, Birnbaum HK. Hydrogen embrittlement of a metastable β-titanium alloy. Acta Mater 2004;52:4161–75. https://doi.org/10.1016/j.actamat.2004.05.030.
[18] Tal-Gutelmacher E, Eliezer D. The hydrogen embrittlement of titanium-based alloys. Jom 2005;57:46–9. https://doi.org/10.1007/s11837-005-0115-0.
[19] Young GA, Scully JR. Hydrogen Embrittlement of Solution Heat-Treated and Aged β-Titanium Alloys Ti-15% V-3% Cr-3% Al-3% Sn and Ti-15% Mo-3% Nb-3% Al. Corrosion 1994;50(12):919–33.

[20] Wei RP, Landes JD. Correlation between sustained-load and fatigue crack growth in high-strength steels. Mater Res Stand 1969.
[21] Wei RP, Gao M. Reconsideration of the superposition model for environmentally assisted fatigue crack growth. Scr Metall 1983;17(7):959–62.
[22] Austen IM, McIntyre P. Corrosion fatigue of high-strength steel in low-pressure hydrogen gas. Met Sci 1979;13:420–8. https://doi.org/10.1179/msc.1979.13.7.420.
[23] Ramsamooj DV, Shugar TA. Modeling of corrosion fatigue in metals in an aggressive environment. Int J Fatigue 2001;23:301–9. https://doi.org/10.1016/s0142-1123(01)00139-6.
[24] Kang DH, Lee JK, Kim TW. Corrosion fatigue crack propagation of high-strength steel HSB800 in a seawater environment. Procedia Eng 2011;10:1170–5. https://doi.org/10.1016/j.proeng.2011.04.195.
[25] Wang R. A fracture model of corrosion fatigue crack propagation of aluminum alloys based on the material elements fracture ahead of a crack tip. Int J Fatigue 2008;30:1376–86. https://doi.org/10.1016/j.ijfatigue.2007.10.007.
[26] Weng L, Zhang J, Kalnaus S, Feng M, Jiang Y. Corrosion fatigue crack growth of AISI 4340 steel. Int J Fatigue 2013;48:156–64. https://doi.org/10.1016/j.ijfatigue.2012.10.015.
[27] Silling SA. Reformulation of elasticity theory for discontinuities and long-range forces. J Mech Phys Solids 2000;48:175–209. https://doi.org/10.1016/S0022-5096(99)00029-0.
[28] Karpenko O, Oterkus S, Oterkus E. Peridynamic investigation of the effect of porosity on fatigue nucleation for additively manufactured titanium alloy Ti6Al4V. Theor Appl Fract Mech 2021;112:102925.
[29] Zhang G, Le Q, Loghin A, Subramaniyan A, Bobaru F. Validation of a peridynamic model for fatigue cracking. Eng Fract Mech 2016;162:76–94. https://doi.org/10.1016/j.engfracmech.2016.05.008.
[30] Karpenko O, Oterkus S, Oterkus E. Investigating the Influence of Residual Stresses on Fatigue Crack Growth for Additively Manufactured Titanium Alloy Ti6Al4V by using Peridynamics. Int J Fatigue 2021;155:106624. https://doi.org/10.1016/j.ijfatigue.2021.106624.
[31] Hu YL, Madenci E. Peridynamics for fatigue life and residual strength prediction of composite laminates. Compos Struct 2017;160:169–84. https://doi.org/10.1016/j.compstruct.2016.10.010.
[32] Chen Z, Bobaru F. Peridynamic modeling of pitting corrosion damage. J Mech Phys Solids 2015;78:352–81. https://doi.org/10.1016/j.jmps.2015.02.015.
[33] De Meo D, Diyaroglu C, Zhu N, Oterkus E, Siddiq MA. Modelling of stress-corrosion cracking by using peridynamics. Int J Hydrogen Energy 2016;41:6593–609. https://doi.org/10.1016/j.ijhydene.2016.02.154.
[34] Silling SA, Askari E. A meshfree method based on the peridynamic model of solid mechanics. Comput Struct 2005;83:1526–35. https://doi.org/10.1016/j.compstruc.2004.11.026.
[35] Madenci E, Oterkus E. Peridynamic Theory and Its Applications. Springer New York Heidelberg Dordrecht London; 2014. DOI 10.1007/978-1-4614-8465-3.
[36] Silling S, Askari A. Peridynamic model for fatigue cracks; 2014.
[37] Silling SA, Bobaru F. Peridynamic modeling of membranes and fibers. Int J Non Linear Mech 2005;40:395–409. https://doi.org/10.1016/j.ijnonlinmec.2004.08.004.
[38] Rimoli JJ. A Computational Model for Intergranular Stress Corrosion Cracking Thesis by 2009;2009:127.
[39] Fisher JC. Calculation of diffusion penetration curves for surface and grain boundary diffusion. J Appl Phys 1951;22:74–7. https://doi.org/10.1063/1.1699825.
[40] Neikter M. Microstructure and hydrogen embrittlement of additively manufactured Ti-6Al-4V. 2019.
[41] Hardie D, Ouyang S. Effect of hydrogen and strain rate upon the ductility of mill-annealed Ti6A14V. Corros Sci 1999;41:155–77. https://doi.org/10.1016/S0010-938X(98)00109-7.
[42] Hondros ED, Seah MP. Theory of Grain Boundary Segregation in Terms of Surface Adsorption Analogues. Met Trans A 1977;8A:1363–71. https://doi.org/10.1007/BF02642850.
[43] Zaccariotto M, Mudric T, Tomasi D, Shojaei A, Galvanetto U. Coupling of FEM meshes with Peridynamic grids. Comput Methods Appl Mech Eng 2018;330:471–97. https://doi.org/10.1016/j.cma.2017.11.011.
[44] Baragetti S, Villa F. Corrosion fatigue of high-strength titanium alloys under different stress gradients. Jom 2015;67:1154–61. https://doi.org/10.1007/s11837-015-1360-5.
[45] Jaske CE, Payer JH, Balint VS. Corrosion Fatigue of Metals in Marine Environments. MCIC Rep (Metals Ceram Inf Center) 1981.
[46] Van Hooreweder B, Moens D, Boonen R, Kruth JP, Sas P. Analysis of fracture toughness and crack propagation of Ti6Al4V produced by selective laser melting. Adv Eng Mater 2012;14:92–7. https://doi.org/10.1002/adem.201100233.
[47] Dawson DB, Pelloux RM. Corrosion Fatigue Crack Growth of Titanium Alloys in Aqueous Environments. Met Trans 1974;5:723–31. https://doi.org/10.1007/BF02644669.
[48] Kok Y, Tan XP, Wang P, Nai MLS, Loh NH, Liu E, et al. Anisotropy and heterogeneity of microstructure and mechanical properties in metal additive manufacturing: A critical review. Mater Des 2018;139:565–86.
[49] Borrego LP, De Jesus J, Ferreira JAM, Costa JD, Capela C. Environmental effect on the fatigue crack propagation of AM TiAl6V4 alloy specimens. Procedia Struct Integr 2019;17:562–7. https://doi.org/10.1016/j.prostr.2019.08.075.